

## Optical-Magnetometry-Based Current Source


Peter A. Koss<sup>1,2,\*</sup>, Reza Tavakoli Dinani<sup>2,†</sup>, Luc Bienstman,<sup>3</sup> Georg Bison<sup>4</sup>, and Nathal Severijns<sup>2</sup>

<sup>1</sup>*Fraunhofer Institute for Physical Measurement Techniques IPM, Freiburg 79110, Germany*

<sup>2</sup>*Instituut voor Kern- en Stralingsfysica, University of Leuven, Leuven B-3001, Belgium*

<sup>3</sup>*Faculty of Engineering Technology, University of Leuven, Leuven B-3001, Belgium*

<sup>4</sup>*Paul Scherrer Institute, Villigen 5232, Switzerland*

 (Received 23 November 2020; revised 19 March 2021; accepted 8 June 2021; published 6 July 2021)

We present a current-monitoring system based on optical magnetometry, which is able to discriminate true current variations from environmental effects at room temperature. The system consists of a dedicated thermally stable magnetic-field-confining coil and an array of four optically pumped magnetometers arranged in a two-dimensional gradiometer configuration. These magnetometers monitor magnetic field variations inside the coil, which correlate with the variations of the driving current of the coil. The system uses a digital signal-processing unit to extract and record in real time the magnetic field values measured by the magnetometers, which allows real-time monitoring of the current. The coil of the system, which is made out of printed circuit boards, can easily be changed to adapt the current-to-field conversion. Thus, we can expand the applicability of this system to a wide range of currents. By using this system to actively feedback control a current source, we stabilize a current of 20 mA on a level better than  $5 \times 10^{-9}$  for an integration time of 70 min.

DOI: [10.1103/PhysRevApplied.16.014011](https://doi.org/10.1103/PhysRevApplied.16.014011)

### I. INTRODUCTION

The system discussed in this paper has been developed for an experiment searching for the permanent electric dipole moment of the neutron (nEDM) [1,2]. The spectrometer, located at the Paul Scherrer Institute (PSI) in Switzerland, uses the Ramsey method of time-separated oscillating fields [3]. This method requires a very stable and low-noise magnetic field during its measurement cycles. In the PSI experiment, a coil powered by a custom-made current source generates this magnetic field. The stability and noise level in the measurement volume of the experiment is ultimately limited by the shield if external disturbances dominate. Otherwise, it is limited by the stability of this current source. Furthermore, the control of systematic effects is paramount in this type of experiment [4]. The apparatus at the PSI has several magnetometry systems, which monitor variations of the magnetic field *in situ* [5,6]. However, we would like to have additional information on the main magnetic field of the experiment, which we intend to get by monitoring the current generating the main magnetic field.

An ultrastable current source, which can generate and monitor the currents used for fundamental physics searches, can be built in many different ways. The most elementary current source uses a constant-voltage source and a precision resistor. Such a simple design can be improved, for example, using specially designed operational amplifiers and resistor networks [7]. However, this rather straightforward path heavily relies on selecting the highest-quality electronics components available. Currently, the best possible stability of a current in the milliamperere range has been achieved by using a Josephson voltage standard as an external reference to a current source. Such a system has achieved a stability of a few parts per  $10^{-9}$  for a 50-mA current [8]. However, the operation of such a system becomes more cumbersome and expensive by the Josephson voltage standard, which only operates with liquid helium, i.e., by cooling it down to 4 K [9]. Another path toward ultrastable currents is the generation of the current at the single-electron level [10]. This type of current source is particularly interesting, since it strongly suppresses the shot noise on the generated current by using feedback control [11]. The technology behind these “single-electron” current sources is very promising; however, at present they can only be used with low currents, i.e., 1 nA or less [12]. On the opposite side, with currents of a few amperes, an approach to generate a stable current is to use nuclear magnetic resonance (NMR). Such

\*peter.koss@ipm.fraunhofer.de

†reza.tavakolidinani@kuleuven.be

‡These authors contributed equally to this work.

ultrastable currents have been used for a long time in NMR experiments [13,14]. This has been made possible by the so-called field-frequency-locking technique [15]. There, a magnetometer lies in the measurement volume of the NMR apparatus. The reading of this magnetometer serves as the input to a feedback-control system. Thus, the field of the NMR experiment is stabilized to the limits in sensitivity of the magnetometer.

In this paper, we propose a method that is similar to the field-frequency locking of NMR, but monitors the magnetic field produced by the current outside the measurement volume of the main experiment. We investigate the sensitivity of a current-monitoring system based on optically pumped magnetometers (OPMs). The main motivation for this work lies with the high sensitivity of OPMs in measuring magnetic fields and to convert this attribute to a high sensitivity in measuring currents [16,17]. To achieve this goal, the system is based on a specially designed magnetic-field-confining coil, which is made out of printed circuit boards (PCBs). This allows the path of the wires and the coil constant to be adapted to a specific application [18,19]. This coil contains an array of four OPMs, each placed in a different section of the coil, which monitor the local field generated by the current passing through it. In this work, we use cesium- (Cs) and potassium- (K) based OPMs and compare their performance for our application. This system, used with a feedback control, can generate an ultrastable current. We present the results of an actively stabilized current of 20 mA, which shows a stability better than  $5 \times 10^{-9}$  for an integration time of 70 min.

## II. EXPERIMENTAL SETUP

The system described in this paper, which is shown schematically in Fig. 1, confines four Cs or K magnetometer modules inside a field-confining coil. A  $\mu$ -metal shield with four concentric cylindrical layers isolates the magnetometers from external electromagnetic interference. A commercial current source drives the current in the coil. This generates a circumferential static magnetic field  $\mathbf{B}_0$  such that each opposing magnetometer pair senses an antiparallel  $\mathbf{B}_0$  as shown in Figs. 1 and 2.

Each magnetometer has its own rf coil, pump, and probe laser beam, which allows us to operate them in an rf-pulsed mode (see Fig. 3). The circularly polarized pump beam orients the atomic spins along the local magnetic field  $\mathbf{B}_j$ . The spin precession of the alkali atoms at the Larmor frequency  $f_L$  is monitored using a low-power circularly polarized probe beam. The signal provided by the magnetometers is a photodiode current, which converts to a voltage signal via a transimpedance amplifier before being digitized by an analog-to-digital converter (ADC).

The Larmor frequency  $f_L$  can be extracted from the digitized signal in real time, using a digital signal-processing unit (DSP), which we call the online mode of analysis. Alternatively,  $f_L$  can be extracted in an offline mode in which signals are stored on a computer and then fitted with an exponentially decaying sinusoid function. We call this the offline mode of analysis. Either method yields Larmor frequencies  $f_L$ , which are used to infer  $i$ , the current passing

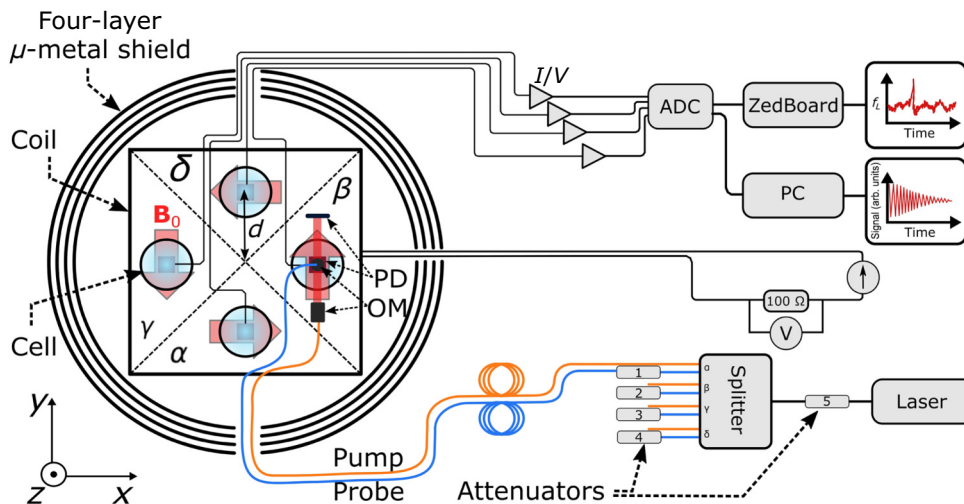


FIG. 1. An overview of the current-monitoring system (not to scale). Each of the four magnetometers is placed at the center of one of the four quadrants ( $\alpha$ ,  $\beta$ ,  $\gamma$ , and  $\delta$ ) of the field-confining coil. This coil stands inside a four-layer cylindrical magnetic shield. The magnetometers measure the magnitude of the static magnetic field  $|\mathbf{B}_j|$  generated by the coil in quadrant  $j$ . The red arrows show the direction of  $\mathbf{B}_j$ . The optical part of the system contains a laser, attenuators, an eight-way beam splitter, optical fibers, optical modules (OMs), and photodiodes (PDs). It allows us to pump and probe all four magnetometers separately and simultaneously.



FIG. 2. Photographs of the field-confining coil used in this work. It is entirely made out of printed circuit boards (PCBs). On the left, the full coil is shown with  $\alpha$ ,  $\beta$ ,  $\gamma$ , and  $\delta$  quadrants, which open via nonmagnetic PCB headers (long white connectors). The arrows on the top panel show the direction of the magnetic field when applying a positive current. On the right, an open quadrant with the mount and a Cs magnetometer is shown. The fibers and cables used for the magnetometer leave the coil through a hole in the top. Temperature sensors (DS18B20; white spots in the mount) are glued into the mount on the top and bottom.

through the coil:

$$i = \frac{2\pi}{\gamma_F \lambda} f_L, \quad (1)$$

where  $\lambda$  is the coil constant and  $\gamma_F$  is the gyromagnetic ratio of the hyperfine ground-state level of the respective alkali atoms. The gyromagnetic ratio of the ground state in alkali atoms with electronic spin  $J$ , nuclear spin  $I$ , and atomic spin  $F$  can be derived from the electronic ( $g_J$ ) and nuclear ( $g_I$ )  $g$  factors of the ground state [20] using

$$g_F = \frac{g_J F(F+1) + J(J+1) - I(I+1)}{2 F(F+1)} + \frac{g_I F(F+1) - J(J+1) + I(I+1)}{2 F(F+1)} \quad (2)$$

and

$$\frac{\gamma_F}{2\pi} = g_F \frac{\mu_B}{h}, \quad (3)$$

where  $\mu_B$  is the Bohr magneton,  $h$  is Planck's constant, and  $g_F$  is the atomic  $g$  factor. For the Cs ground state  $6^2S_{1/2}$  with spin  $F = 4$ , the gyromagnetic ratio is  $\gamma_4/2\pi = 3.498\,620\,95(35)$  Hz/nT. In a similar way, we use the  $4^2S_{1/2}$  K ground state with spin  $F = 2$ , the gyromagnetic ratio of which is  $\gamma_2/2\pi = 7.004\,660\,13(84)$  Hz/nT. Thus, this is an attempt to link a current measurement to atomic constants.

### A. Field-confining coil

The requirements on the coil for this current-monitoring concept are linked to the type of magnetometry we are using. The coil has to produce a very uniform magnetic

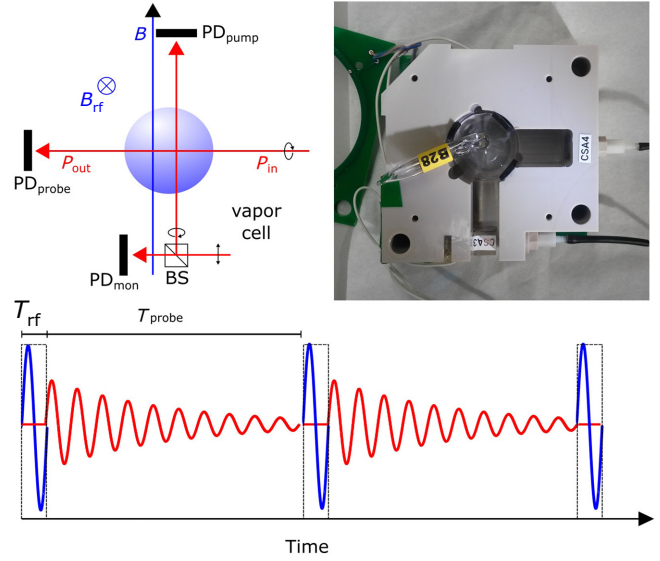


FIG. 3. A schematic and photograph of the optically pumped magnetometer (OPM) used for this work. The top left schematic represents an OPM module, where the red arrows represent the laser beams, the three photodiodes are labeled PD, and BS is a beam splitter. The pump beam is parallel to the applied magnetic field and the probe beam is perpendicular to the pump beam. The top right photograph shows a Cs OPM, the frame of which is made out of polyether ether ketone (PEEK). The vapor cell (labeled B28) is paraffin coated. CSA3 and CSA4 are circularly polarizing optics. The green PCB is one of two coils, which are arranged like Helmholtz coils. The bottom schematic shows the operational pulse sequence for these OPMs. A short, typically 1–3-cycle-long rf pulse is applied on the spin-polarized medium of the sensor (the blue pulse). This initiates free spin precession, which the probe beam monitors (the red signal). Note that, for clarity, the frequencies and amplitudes are not to scale.

field, as gradients broaden the magnetic resonance lines of the magnetometer. This broadening degrades the sensitivity of the magnetic field reading [21]. The coil also has to confine the field within itself such that the stray field is not affected by the environment. The most important criterion for our application is the gradiometer configuration of the magnetometers, as we want to suppress environmental magnetic field perturbations. The field direction inside the coil should be circumferential. This allows us to have antiparallel magnetic fields for pairs of magnetometers that are sensitive along the  $x$  and  $y$  directions (see Fig. 1). We have a total of four magnetometers, each installed in a separate quadrant of the coil. In the presence of a coil driving current  $i(t)$  and an external perturbing magnetic field  $\mathbf{B}_{\text{ext}}(x, y, t)$ , where we assume that  $\mathbf{B}_{\text{ext}}$  is a function of time and the coordinates  $(x, y)$ , the magnetic field measured by the magnetometers at a time  $t$  is

$$\mathbf{B}_j(x, y, t) = \mathbf{B}_{\text{coil},j}(x, y, t) + \mathbf{B}_{\text{ext},j}(x, y, t), \quad (4)$$

where the index  $j$  denotes the module:  $j = \alpha, \beta, \gamma, \delta$ .

Taking the simplified case where  $\mathbf{B}_{\text{ext}}$  has constant gradients along  $x$  and  $y$ , we obtain

$$\text{pair 1} = \begin{cases} B_\alpha \simeq i\lambda_\alpha + (B_{\text{ext},0} - dB'_y), \\ B_\delta \simeq i\lambda_\delta - (B_{\text{ext},0} + dB'_y), \end{cases} \quad (5)$$

$$\text{pair 2} = \begin{cases} B_\beta \simeq i\lambda_\beta + (B_{\text{ext},0} + dB'_x), \\ B_\gamma \simeq i\lambda_\gamma - (B_{\text{ext},0} - dB'_x), \end{cases} \quad (6)$$

where we group the sensors by opposing gradiometer pairs.  $B_{\text{ext},0}$  is the magnitude of the perturbing field at the origin.  $B'_x = (\partial B_{\text{ext}}/\partial x)(0,0)$  and  $B'_y = (\partial B_{\text{ext}}/\partial y)(0,0)$  are the field gradients at the origin. The parameter  $d$  is the distance of the center of the vapor cell of the magnetometer from the origin of the coordinate system, which is located at the center of the coil. The factors  $\lambda_\alpha$ ,  $\lambda_\beta$ ,  $\lambda_\gamma$ , and  $\lambda_\delta$  are the coil constants at the locations of the magnetometers. They can be measured accurately.

Using Eqs. (5) and (6), the driving current of the coil reads

$$i(t) = \frac{\sum_j B_j + 2d(B'_x - B'_y)}{\sum_j \lambda_j}, \quad (7)$$

which shows that this gradiometer configuration can suppress a uniform  $\mathbf{B}_{\text{ext}}$ . Higher coil constants and smaller dimensions of the coil suppress the influence of the constant gradients. However, for higher-order nonuniform cases, we require more information about the first-order gradient of  $\mathbf{B}_{\text{ext}}$  along the  $x$  and  $y$  axes. This can be achieved by installing a third magnetometer along these axes. For the investigation in this paper, we limit ourselves to only two magnetometers per axis.

The maximum contribution of  $\mathbf{B}_{\text{ext}}$  to a current measurement of one sensor, including the first-order gradient, is  $(B_{\text{ext},0} + dB')/\lambda$ . Using Eq. (7) and assuming the same coil constant  $\lambda$  and the same magnitude of gradients for all quadrants, this contribution is  $dB'/2\lambda$ . One can use the ratio of these contributions to define a shielding factor associated with the gradiometer configuration of the coil. This defines the extent to which the effect of  $\mathbf{B}_{\text{ext}}$  on the measured current is suppressed. So,

$$S = 2(B_{\text{ext},0}/dB' + 1). \quad (8)$$

The factor of 2 in  $S$  comes from the two pairs of magnetometers. This factor is unity when we only use one pair of magnetometers. Thus, Eq. (8) shows how a two-dimensional gradiometer configuration can outperform a one-dimensional configuration. To improve  $S$ , it is clear that  $d$  should be reduced.

The coil used in this work is shown in Fig. 2. It is entirely made out of multilayered PCBs. Each quadrant has 100 equidistant current loops. The magnetic field is

perpendicular to those current loops and points in different directions in each quadrant. The four quadrants open separately, with the use of removable front panels. These front panels are connected to the body of the coil with non-magnetic PCB headers (females, Molex KK 4455 series; males, Molex 5046 series). Each of these quadrants contains a mount made of PFCC201, a nonmagnetic and low-thermal-expansion material. These mounts are glued into the quadrant using silicon glue. An OPM can be mounted inside each quadrant as shown in Fig. 2. The total resistance of the coil is  $R = 58 \Omega$  and the design coil constant is  $0.5 \mu\text{T}/\text{mA}$ . The characteristics of the coil design used in this work are similar to a coil design presented before [18].

The coil must be robust against temperature fluctuations, as this can affect all four quadrants in the same way; thus generating a fake current drift. A simple aluminum thermal chamber, which is heated with silicon oil, is used for all measurements associated with K magnetometers and keeps the operating temperature at 330 K. All measurements associated with Cs magnetometers are performed at room temperature. The aluminum chamber accommodates the coil. In order to fit this assembly inside the innermost layer of the magnetic shield, a volume of  $40 \times 40 \times 40 \text{ cm}^3$  is required. This setup allows us to make dedicated measurements of the coil constant as a function of temperature. We determine that a relative change in the coil constant is less than  $4 \times 10^{-5} \text{ K}^{-1}$ . At room temperature, we measure a temperature stability of 0.1 mK after 2 min and 10 mK after 1 h. Thus, with this thermally stable coil constant, we do not expect any perturbing temperature effects on the relevant time scales.

## B. Magnetometers

The magnetometers used in this work are optically pumped magnetometers. They are based on the detection of a magnetic resonance signal in a spin-polarized vapor of alkali metals [22]. Their relative simplicity of use and very high sensitivity have made them a very popular tool in fundamental physics searches [23,24]. Figure 3 shows the magnetometer modules used for this work. Two different elements are chosen and used in different modules for comparison: Cs and K. The alkali-metal vapor of these modules is contained in a paraffin-coated glass cell. This coating prevents depolarization of the vapor through collisions of the atoms with the glass wall [25,26].

The laser light used for the optical pumping of the medium is provided by two single-mode diode lasers from TOPTICA. The wavelength of one is stabilized to the  $F = 2 \rightarrow F' = 1$  transition of the K  $D_1$  line, i.e., at 770 nm. The other laser is stabilized to the  $F = 4 \rightarrow F' = 3$  transition of the Cs  $D_1$  line, i.e., at 894 nm. The stabilization of the laser wavelength is performed with the use of a Doppler-free saturation spectroscopy setup. The laser light is guided to the module via multimode fibers. At the end of

these fibers, a beam-collimating optical module (OM) with a linear polarizer is mounted. Another linear polarizer is part of the circularly polarizing optics (CSA3 and CSA4 in Fig. 3). By changing the alignment of these polarizers, one can continuously change the laser power passing through the vapor cell of the magnetometer.

The OPMs presented here use the so-called free-spin-precession (FSP) mode of operation [27]. This consists of polarizing the alkali vapor with a pumping beam and then monitoring the free precession of the spin-polarization of the alkali vapor. This is in contrast with other modes, e.g., the very popular  $M_x$  type, which continuously drives the magnetic resonance [28]. The advantages of this FSP mode are much lower systematic effects on the readout of the Larmor frequency, less crosstalk between the rf fields of the modules, and good sensitivity. This FSP mode typically reaches levels lower than  $100 \text{ fT}/\sqrt{\text{Hz}}$  in the shot-noise limit [27].

In our case, the FSP is initiated with a tipping  $\pi/2$  pulse [29,30]. This pulse is typically 1–3 periods of a resonant rf pulse of large amplitude. Since it is very short in time, it is very broad in the frequency domain. The advantage is that the frequency of the pulse does not have to be very close to the Larmor frequency of the alkali vapor. This tipping pulse typically occurs every 100 ms, which sets a 10-Hz sampling rate for the current measurement. Higher sampling rates are possible, but this will degrade the sensitivity of the magnetometers. The FSP signal recorded by the photodiode is amplified by a transimpedance amplifier, the nominal gain of which is  $G = 10^6 \text{ V/A}$ . This voltage signal is digitized using either a 16-bit ADC with a maximum sampling rate of 1 MS/s or a 24-bit ADC sampling at 48.8 kS/s. The high-resolution ADC is used in the online mode of analysis, while the lower-resolution one is used in the offline mode.

The digitized signal is an exponentially decaying sinusoidal time series. For a given sampling rate  $r_s$ , with  $r_s/2 \geq f$ , the recorded voltage reads

$$V = \begin{cases} V(n) &= V_0 \sin(2\pi f_L n \Delta t + \phi) e^{-\Gamma n \Delta t} + w(n), \\ n &= 0, 1, 2, \dots, N-1, \end{cases} \quad (9)$$

where  $f_L$  is the Larmor frequency,  $\Gamma$  is the relaxation rate imposed by the experimental conditions, and  $\phi$  is the initial phase. The signal is perturbed by white noise  $w(n)$  and sampled with a sampling interval of  $\Delta t = 1/r_s$ . The total recording time is  $T_r = N/r_s$ .

The statistical sensitivity of the magnetometer depends on the precision with which we can extract the frequency from the measured signal. The statistical tool that gives the lowest variation of an unbiased frequency estimator is the Cramér-Rao lower bound [31]. The Cramér-Rao lower bound for Eq. (9) in terms of experimentally measurable

parameters is [32]

$$\sigma_f = \frac{\sqrt{12}}{(V_0/\rho_V) T_r^{3/2}} \sqrt{C}, \quad (10)$$

where  $V_0/\rho_V$  is the signal-to-noise ratio,  $T_r$  is the length of the signal, and  $C$  is given by

$$C = \frac{N^3}{12} \frac{(1-z^2)^3 (1-z^{2N})}{z^2 (1-z^{2N})^2 - N^2 z^{2N} (1-z^2)^2}, \quad (11)$$

where  $z = e^{-\Gamma \Delta t}$ . We characterize the sensitivity of the magnetometers in the shot-noise limit. This means that the noise level in Eq. (10) is given by  $\rho_V = G \sqrt{2e I_{dc}}$ , where  $e$  is the electron charge,  $G$  is the gain of the transimpedance amplifier, and  $I_{dc}$  is the dc part of the photodiode current.

The sensitivity of the FSP mode depends on the atomic physics parameters of Cs and K in a nontrivial way [27]. For this reason, we scan the laser powers of the pump and the probe beam in order to map the sensitivity and find the optimal operation point. The results of this investigation are shown in Fig. 4 for a  $1 \mu\text{T}$  holding field. The sensitivity of the magnetometers is given by the Cramér-Rao lower bound in Eq. (10). The only parameter degraded by the field strength is the line width of the signal  $\Gamma$ . Figure 5 shows the dependence of the line width of the Cs and K magnetometers as a function of the applied magnetic field strength. The cell diameter for the Cs magnetometer is 30 mm and for K the values are 40 mm and 70 mm. Cs magnetometers are used at room temperature ( $23^\circ\text{C}$ ) but K magnetometers are used at  $51$  and  $47^\circ\text{C}$ . The higher operating temperature for K is necessary because the vapor pressure of K is much lower than that of Cs. The measurements all use the PCB coil of Fig. 2. We clearly see how the

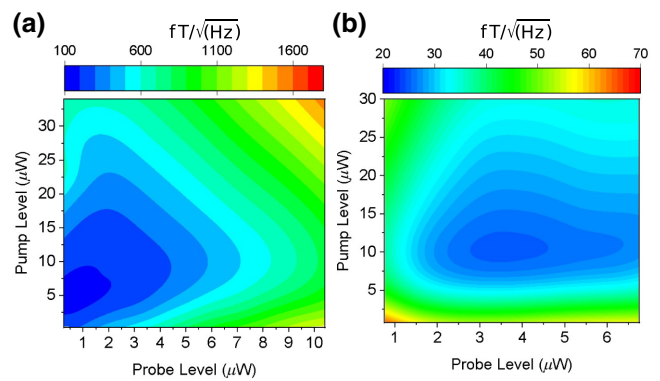


FIG. 4. Shot-noise limited sensitivity maps as a function of the laser power at  $1 \mu\text{T}$  for Cs and K. (a) A Cs magnetometer held at room temperature with a vapor-cell diameter of 30 mm. (b) A K magnetometer held at  $50^\circ\text{C}$  with a vapor-cell diameter of 70 mm. The experimentally determined maximum sensitivity lies at  $180 \text{ fT}/\sqrt{\text{Hz}}$  for Cs and  $20 \text{ fT}/\sqrt{\text{Hz}}$  for K magnetometers. In both cases, the FSP signal duration is 70 ms.

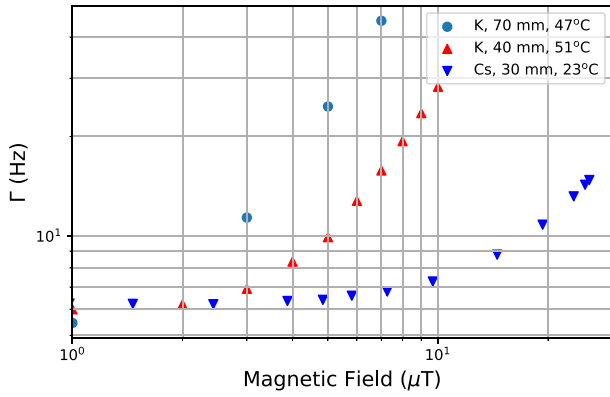


FIG. 5. The line width of the Cs and K free-spin-precession (FSP) signals as a function of the applied magnetic field strength. The line width at  $1 \mu\text{T}$  is close to the intrinsic line width of the cells [33]. At higher fields, the line width of the FSP signal broadens due to the nonlinear Zeeman effect and the magnetic field gradients. The diameter of the cell is indicated in millimeters for each case.

line width is very strongly influenced by the field strength in the case of a 70-mm-diameter K vapor cell. This behavior can be improved by using a smaller vapor cell, e.g., a 40-mm-diameter one. This means that K is very sensitive to magnetic field gradients even at low magnetic field strengths [21,34]. In comparison, Cs is much more robust to magnetic field gradients. Other parameters that affect the line-width broadening can be explained by the nonlinear Zeeman effect, which are described by the Breit-Rabi formula [35]. This effect is shown in Fig. 6 for both Cs and K. Over the same range of magnetic field strengths, this effect is larger by more than an order of magnitude for K. At  $1 \mu\text{T}$ , where the effect of gradients and the nonlinear

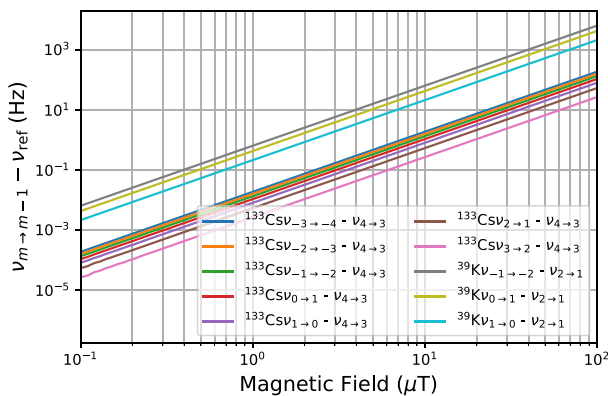


FIG. 6. The nonlinear Zeeman effect in potassium ( $^{39}\text{K}$ ) with  $F = 2$  and cesium ( $^{133}\text{Cs}$ ) with  $F = 4$ , i.e., nonlinear splitting of the magnetic sublevels, denoted by  $m$ . The large linear contribution of the Zeeman effect is subtracted by using one sublevel as a reference ( $\nu_{4 \rightarrow 3}$  and  $\nu_{2 \rightarrow 1}$ ). The effect is much larger in the case of potassium due to a smaller hyperfine splitting of the element.

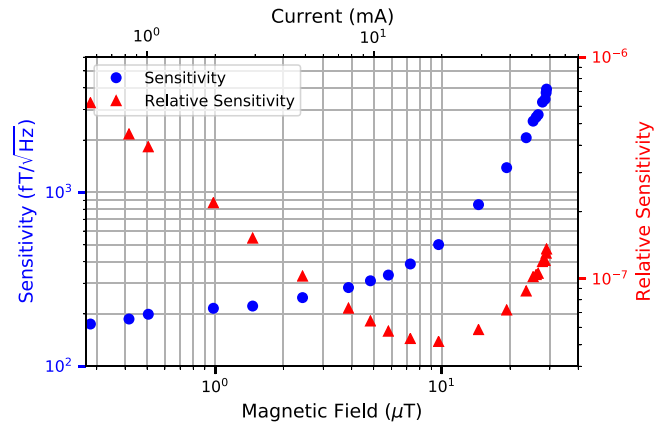


FIG. 7. The shot-noise-limited ( $\bullet$ ) and relative ( $\blacktriangle$ ) sensitivities of the Cs magnetometers used in the system as a function of the magnetic field and current. The relative sensitivity is shown for a 1-Hz bandwidth. The sensitivity is limited at high magnetic fields due to Cs line broadening.

Zeeman effect are minimized, the difference in decay rates may be explained by different cell-coating qualities [26]. Although the tested K magnetometer is more sensitive than the Cs magnetometer, the magnetic field dependent line-width broadening limits its sensitivity. As our application typically requires currents of 12 mA or more, corresponding to a field of  $6 \mu\text{T}$  in the coil, we decide to use Cs magnetometers for the current measurements.

Figure 7 shows the shot-noise-limited ( $\sigma_{\text{SN}}$ ) and relative ( $\sigma_{\text{rel}}$ ) sensitivities of the Cs magnetometers as a function of the magnetic field in the coil. At low fields, where the line-width broadening is small,  $\sigma_{\text{SN}}$  worsens moderately. However, due to line-width broadening,  $\sigma_{\text{SN}}$  gets worse at higher fields. The relative sensitivity improves up to  $10 \mu\text{T}$ , where we see  $\sigma_{\text{rel}} = 5 \times 10^{-8}$ . This corresponds to a sensitivity of 1 nA on a 20-mA current applied to the coil.

### C. Digital signal processing

We develop a DSP system to extract the precession frequency  $f_L$  of Cs atoms in all four magnetometers simultaneously and in real time. The core of the system is a ZedBoard [36], which is a prototyping board featuring a highly integrated system on a chip (SOC). The input of the DSP is a 24-bit ADC with a sampling rate of 48 kS/s. This DSP system can accept up to eight input channels, where the input signal is an amplified analog FSP voltage signal.

The digitized signal is filtered, amplified, and then demodulated, using a lock-in algorithm, to extract the instantaneous phase  $\theta(t)$  of the signal compared to a local oscillator. By knowing the accumulated phase  $\theta(t)$  as a function of time, one can find the frequency  $f_L$  using a linear regression. To keep track of  $f_L$  over time, a proportional-integral-differential (PID) algorithm is used.

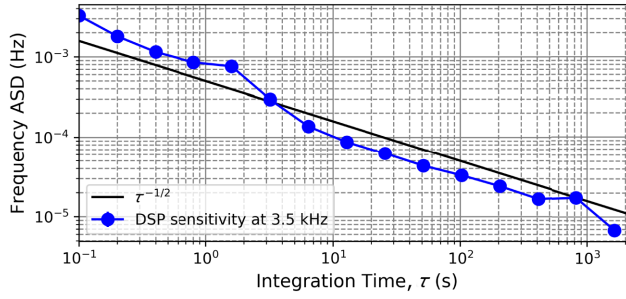


FIG. 8. The Allan standard deviation (ASD) of the measured frequency of a continuous test sinusoidal signal using our DSP system at 3.5 kHz. At an integration time of 0.5 s, it has a sensitivity of 1 mHz at 3.5 kHz. The lines between the points are merely a guide for the eye.

The associated error signal in the PID algorithm is the difference between the measured frequency and the presumed stable local oscillator frequency. Both the demodulation and PID algorithms are implemented on the field-programmable gate array (FPGA) of the ZedBoard. The linear regression of the phase as a function of time is implemented on the processor of the ZedBoard. This allows us to calculate the Larmor frequency  $f_L$  of a typically 70-ms-long FSP signal from all four modules in less than 30 ms.

We evaluate the sensitivity of this DSP system at 3.5 kHz using a continuous sinusoidal test signal generated at an amplitude comparable to the average rms value of a standard FSP signal. The test signal is generated by a Zurich Instrument lock-in amplifier model MLFI. Figure 8 shows the modified Allan standard deviation (ASD) of the measured 3.5 kHz frequency as a function of the integration time  $\tau$ . All Allan plots in this paper use the so-called modified Allan standard deviation, as it yields much better confidence intervals at high integration times [37]. The sensitivity of the DSP system is limited by pure white noise, as is clear from the straight line with slope  $\tau^{-1/2}$ . One expects to measure the frequency of a clean test signal with a sensitivity of about  $1 \text{ mHz}/\sqrt{\text{Hz}}$  using our DSP system.

We also compare the frequencies measured by the DSP system with an offline numerical analysis using an exponentially decaying sinusoidal fit function. Figure 9 shows the performance of the DSP and the offline analysis for a duration of 1 h. At short  $\tau$ , the offline numerical analysis shows better performance. As  $\tau$  becomes larger than 20 s, both methods show the same result. At large values of  $\tau$ , where the offline mode of analysis takes a long time to compute  $f_L$  for all data points, the DSP system is much more efficient. Figure 9 also shows a sensitivity of  $700 \text{ fT}/\sqrt{\text{Hz}}$ . This is about 3.5 times larger than  $\sigma_{\text{SN}}$ . By reducing environmental noise, one expects to reach  $\sigma_{\text{SN}}$ .

Note that the DSP system is fast to track frequency variations but its performance is limited to the specific

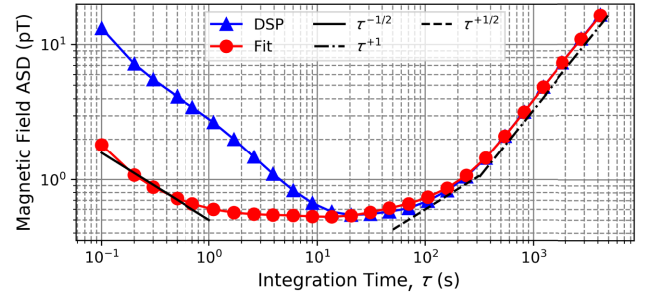


FIG. 9. The ASD plot of the measured magnetic field inside our coil using Cs magnetometers at  $1 \mu\text{T}$  and at room temperature. The FSP signals of the magnetometers are analyzed using the DSP system ( $\blacktriangle$ ) and a least-squares fitting method ( $\bullet$ ). The solid line represents white noise ( $\tau^{-1/2}$  behavior) while the dashed line represents a random walk ( $\tau^{+1/2}$ ) and the dash-dotted line represents long-term drifts ( $\tau^{+1}$  behavior). The lines between the points are merely a guide for the eye.

frequency range defined by the bandwidth of its band-pass filter. In our case, this is  $3500 \pm 200 \text{ Hz}$ . Beyond that range, the DSP system will lose frequency tracking. However, one can still use our DSP to monitor the frequency of demodulated signals. In this way, any high-frequency signals can be demodulated first and then sent to the DSP to extract their frequencies. In order to do that, a lock-in amplifier with a wide bandwidth and with a stable local oscillator oscillating at a frequency 3.5 kHz away from the input signal is required. The output of the lock-in is a demodulated signal oscillating at 3.5 kHz and can be used as the input of our DSP system. In our case, the lock-in amplifier should have four input channels with preferably four independent local oscillators, one for each channel. We use this technique to actively measure the precession frequency of the FSP signals oscillating at 35 kHz when a 20-mA current drives the field coil. Such a DSP system is a promising solution for experiments requiring active and fast analysis of data from multiple sources. It has been used in precision measurements such as the operation of an array of Cs magnetometers in the PSI nEDM experiment [5] or in magnetocardiography [38,39]. The DSP system described here has also served as a prototype for a larger system, since it scales to support additional channels by using an SOC with more resources. The larger system features a 128-channel DSP, using two XCZU9EG boards, which will be used in the next generation of the nEDM experiment at the PSI called n2EDM [1].

#### D. Magnetic shields

For most measurements with Cs magnetometers, we use a four-layer cylindrical  $\mu$ -metal shield to isolate the magnetometers from external electromagnetic interference. The cylinders are closed at one end and open at the other. Each open end has a removable end cap. All layers of

the  $\mu$ -metal shield are manufactured from ASTM A753-08 alloy type 4, with a thickness of 1.6 mm, and are heat treated for maximum magnetic permeability. The layers of the shield are evenly spaced and the innermost layer is 80 cm long, with a diameter of 42 cm. The outermost one is 92 cm long with a diameter of 54 cm. For measurements with K magnetometers, we use the magnetic shield of the nEDM experiment at the PSI [4].

### III. RESULTS

We demonstrate the performance of the system for screening external magnetic interference and for tracking current variations. We also show that this system can detect small modulated currents under unshielded and shielded measurement conditions. Finally, we demonstrate a stabilized current source based on using the two-dimensional gradiometer configuration of four Cs magnetometers and a current feedback-control system.

#### A. Magnetic interference screening

The performance of the system in the presence of an external magnetic interference is evaluated by exposing the coil to the environmental laboratory conditions, i.e., by removing it from the  $\mu$ -metal shield. As the system operates at low magnetic fields, we use three pairs of square Helmholtz coils to compensate the projection of the static component of the background magnetic field along the measurement axes of the coil. Then we evaluate how well  $\mathbf{B}_{\text{ext}}$  is detected and canceled by the system. We test the system at driving currents larger than 10 mA. The system can operate at lower currents if the background field reduces to a level lower than the field generated by the coil.

The background magnetic field gradients degrade the quality of the FSP signal and increase its decay rate. This in turn allows us to increase the sampling rate in current measurements up to 50 S/s. Fig. 10 shows the ASD of the measured driving current of the coil and the screening factor associated with the gradiometer configuration of the coil in an unshielded environment. For this measurement, the coil is driven with a 12-mA current. The screening factor shows the extent to which the ASD of the current averaged over all or some of modules reduces compared to the ASD of the current obtained from a single module. From Fig. 10, we see that the screening associated with all modules outperforms those associated with modules  $\alpha\delta$  and  $\beta\gamma$ . At short integration times ( $\tau = 100$  ms), the screening factor reaches a value of 34. This factor can be as high as 60 for very long integration times. Note that the performance of the system in screening depends on the uniformity of  $\mathbf{B}_{\text{ext}}$ , the design of the coil, and the orientation of modules in respect to  $\mathbf{B}_{\text{ext}}$ . Nevertheless, one expects that the system stability improves by more than one order of magnitude due to the screening effect of the gradiometer configuration.

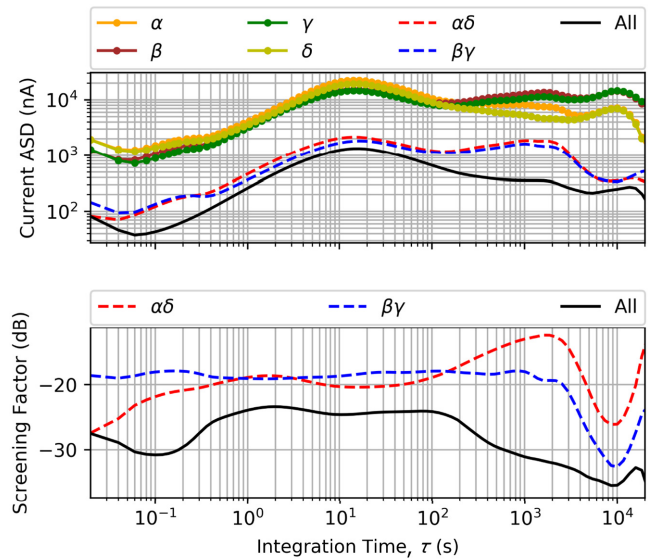


FIG. 10. Top: the ASD plot of the measured current of the coil using Cs magnetometers at room temperature as a function of the integration time. Bottom: the corresponding screening factor of the gradiometer configuration of our system. The coil stands in an unshielded region and it is driven by a 12-mA current. The different traces represent data for different quadrants and combinations of quadrants.

#### B. Current tracking

Figure 11 shows the response of the system to  $\pm 30$ ,  $\pm 60$ , and  $\pm 90$  nA step changes in current passing through the coil. We use the DSP and least-squares fitting methods to analyze the currents sensed by the system. The power of the beams of all four magnetometers is set to the region of optimal sensitivity, as shown in Fig. 4. The magnetometers are placed in the coil at a 1- $\mu$ T magnetic field, which is produced by a 2-mA driving current. The figure also shows how well all magnetometers can track each other in the presence of sudden changes. We find a correlation better than 99.4% between each channel and the average of all four channels. The performance of our system is compared with that of a 7(1/2) digit digital multimeter (DMM) with a sampling rate of 0.5 s<sup>-1</sup> and an integration time of ten 50-Hz power-line cycles. The DMM is used to monitor voltage drops across a 100- $\Omega$  resistor with a 0.2 ppm/ $^{\circ}$ C temperature coefficient. The correlation between the DMM and the system is measured to be 92%. One can note that our system outperforms the DMM, as it shows less deviation from expected values of the current.

#### C. Modulated current

As a test of the viability of the optical magnetometers to monitor small variations in current, we modulate the driving current with a modulation frequency  $f_{\text{mod}}$ . This imprints an alternating pattern on the magnetic field inside the coil. The optical magnetometers are then used to directly



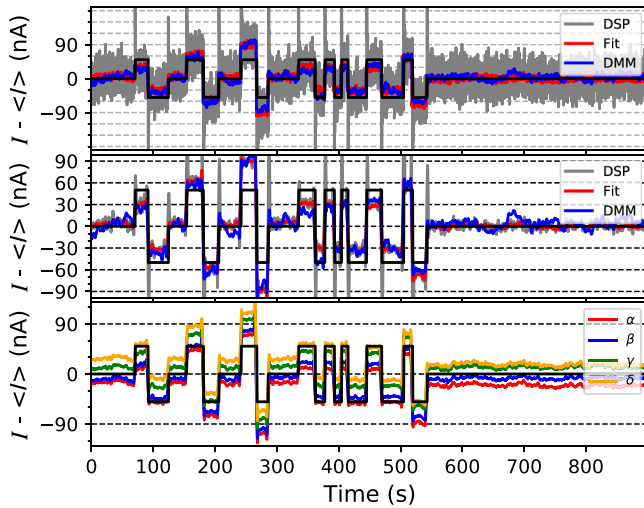


FIG. 11. The response of the system and the DMM to sudden changes in current. The data of the system are analyzed using digital signal processing (DSP) and least-squares fitting (Fit). The top panel shows the system and DMM responses without filtering but the middle panel shows filtered responses using a third-order Savitzky-Golay filter with a window length of 5 s. The bottom panel shows the individual responses of all four Cs magnetometers ( $\alpha$ ,  $\beta$ ,  $\gamma$ , and  $\delta$ ) filtered using the same method as in the middle panel. The individual responses are shifted by small offsets to demonstrate their correlation. The black solid line represents the trigger signal where the current in the coil is changed in discrete steps of  $\pm 30$ ,  $\pm 60$ , and  $\pm 90$  nA. The gray spikes show where the PID of our DSP tries to find the right values after a sudden change in the coil current.

monitor the resulting magnetic field variations and consequently the current variations.  $f_{\text{mod}}$  is limited by the sampling rate of the system. In an unshielded region, where the field nonuniformity is high, the FSP signals decay rapidly. This results in a sampling rate of up to 50 S/s. In a very-well-shielded region, the typical sampling rate is 10 S/s. To achieve a higher sampling rate, we increase the pump and probe laser powers in order to shorten the FSP decay rate. This leads us to acquire at a sampling rate of 50 S/s. At higher sampling rates, the DSP fails to process the FSP signals, as it typically requires 30 ms to process them.

Figure 12 shows recordings of the averaged amplitude of the modulated current, sensed by all magnetometers, when the coil is driven by a 2-mA current. The coil stands in a shielded region with four layers of  $\mu$ -metal. The modulation pattern is a square waveform with a frequency  $f_{\text{mod}} = 0.2$  Hz that activates a mechanical relay with a delay time of 100 ms. The relay connects (disconnects) a secondary current source to (from) the main current source. The former generates nanoampere currents and the latter drives the coil with milliampere currents. The figure shows how a small amplitude of a modulated current can be monitored by the system in a shielded environment using all four modules.

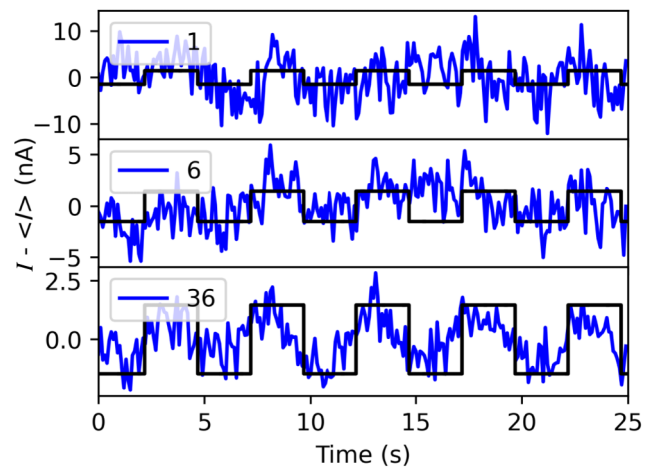


FIG. 12. Modulated current signals with an amplitude of 2 nA acquired at  $f_{\text{mod}} = 0.2$  Hz. Three examples are shown. The top panel shows a single-shot acquisition. The middle panel shows the effect of averaging over six repetitions of this experiment and the bottom panel shows the effect of averaging over 36 repetitions. The square modulation pattern used to turn the nanoampere current on and off is also shown.

To compare the performance of our system in an unshielded and well-shielded region, we calculate the power spectral density (PSD) of the measured current of the coil, which is the sum of a 12-mA dc and a 20-nA current modulated at 1 Hz. We use a standard periodogram method to calculate the PSD. Figure 13 shows the results of the PSD after 1 h of data acquisition. The data show how the PSD is improved when we go from using a single module ( $\alpha$ ) to two ( $\alpha\delta$ ) and four ( $\alpha\beta\gamma\delta$ ) modules. Two and four modules correspond to one-dimensional and two-dimensional gradiometer configurations, respectively. The figure also demonstrates how the two-dimensional configuration in a noisy region, without the use of any magnetic shield, can resolve the modulated signal. This signal appears as a series of spikes at  $f_{\text{mod}} = 1$  Hz and its higher harmonics up to the fifth order. The signal-to-noise ratio (SNR) at  $f_{\text{mod}} = 1$  Hz is about 5. By using a four-layer  $\mu$ -metal shield, we see much improvement in the PSD as expected. It results in a SNR of approximately 95.

#### D. Current feedback control

The current applied to the field coil stabilizes through a feedback-control scheme, which is shown in Fig. 14. In this scheme, the amplified photocurrent signals are first demodulated using a four-input-channel lock-in amplifier with four independent local oscillators. As our DSP system can track signals at  $f_{\text{DSP}} = 3.5$  kHz, we use a lock-in to demodulate the FSP signals oscillating at high frequencies such that the demodulated signals have a frequency close to  $f_{\text{DSP}}$ . Thus, signals at higher frequencies are trackable by our DSP system. In order to achieve that, the lock-in

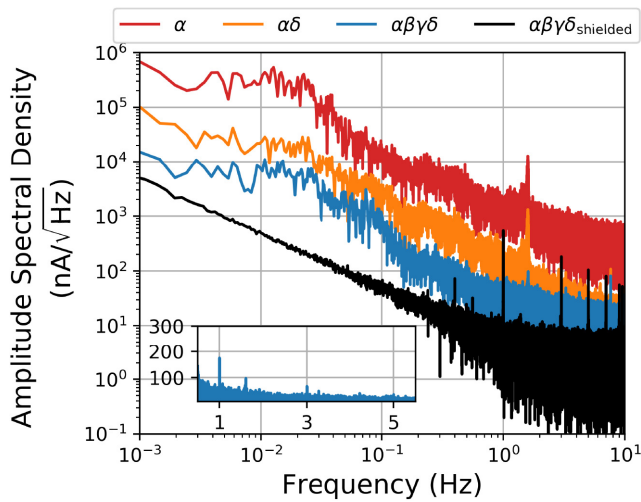


FIG. 13. The amplitude spectral density of the measured current at 12 mA in an unshielded environment after 1 h of data acquisition when a 20 nA modulated current at  $f_{\text{mod}} = 1$  Hz is added to the 12-mA current. The current is measured using modules  $\alpha$  (red) and  $\alpha\delta$  (orange) and all four modules (blue). The black-color data show the performance of the system in a similar measurement using all four modules but in a shielded environment. The spikes at 1 Hz and its odd multiples are associated with  $f_{\text{mod}} = 1$  Hz and higher harmonics. The inset shows an expanded view of the amplitude spectral density for all modules in the unshielded environment on a linear plot.

bandwidth should be wide enough and the frequency of the local oscillators must be shifted from the frequency of the FSP signals by  $f_{\text{DSP}}$ . The typical bandwidth of the lock-in used in our measurements is 4.5 kHz. In the particular case where the current of the coil is 2 mA, the lock-in can be bypassed. The demodulated outputs of the lock-in are first

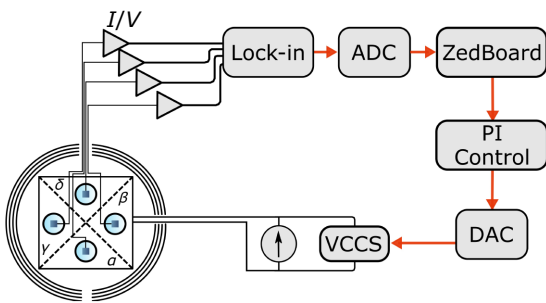


FIG. 14. The signal path for a current feedback-control loop. The amplified photocurrent signals of all four modules are demodulated by a four-input-channel lock-in amplifier with four independent local oscillators. The demodulated output signals of the lock-in are sent to the DSP to measure the driving current of the coil. The output of the proportional-integral (PI) control converts to an analog signal using a digital-to-analog converter (DAC) and is then sent to a voltage-control current source (VCCS). The VCCS output is added to the output of the main current source to compensate current drifts.

digitized. Then they are sent to the DSP system for their frequencies to be extracted. The DSP calculates  $\bar{f}$ , the average of these frequencies, and  $\delta f$ , the deviation of  $\bar{f}$  from  $f_{\text{DSP}}$ .  $\delta f$  is used as the error signal for the current feedback control, which consists of a proportional-integral (PI) control algorithm, a digital-to-analog converter (DAC) and a voltage-controlled current source (VCCS) with a typical gain of 100 nA/V. The VCCS is used to compensate current fluctuations of the main current source.

Figure 15 shows the ASD plot of the current stability when the drift in the coil current is stabilized using the current feedback control. The coil current is 20 mA, which corresponds to a magnetic field of 10  $\mu\text{T}$  inside the coil. We use the offline numerical analysis rather than the online method to calculate the frequencies of the FSP signals and the driving currents corresponding to them. The reason for using the offline method is that it outperforms the online method at short integration times. For comparison, we show the current stability at 20 mA with and without current feedback control. The data associated with each case are recorded at different times but under the same experimental conditions. As Fig. 15 shows, the use of feedback control results in significant improvements of the current stability, especially on the long time scales. The best stability we can achieve is just above  $4 \times 10^{-9}$  after 70 min of averaging. The figure also shows how the stability improves by extending the gradiometer

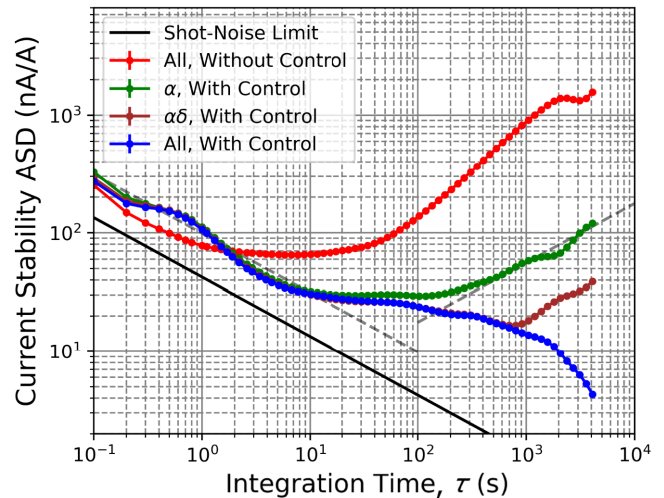


FIG. 15. The ASD plot of the current stability at 20 mA, which corresponds to a magnetic field of 10  $\mu\text{T}$  inside the coil. Cs magnetometers are used to monitor the coil current when no current feedback control is implemented (red) and when the current feedback control is applied but the current is measured using a single (green), two (brown), and all four (blue) magnetometers. The dashed lines represent white noise (left) with  $\tau^{-1/2}$  and random-walk behavior (right) with  $\tau^{+1/2}$ . The solid line shows the best achievable performance based on the shot-noise-limited sensitivity of the Cs magnetometers.

feature from one pair to two pairs of magnetometers. The current stability based on using a single ( $\alpha$ ) and a pair ( $\alpha\delta$ , one-dimensional gradiometer) of Cs magnetometers starts to drift after 200 and 800 s. However, using two pairs of Cs magnetometers, which corresponds to a two-dimensional gradiometer configuration, it continues to improve even after 1 h of averaging. This shows how well a two-dimensional gradiometer configuration can screen the effect of external magnetic interference. The deviation from a typical  $\tau^{-1/2}$  behavior around 10 s could be due to the stability of the reference oscillator. The technical implementation of this system could still be slightly improved, as the sensitivity of the magnetometers is worse than the shot-noise-limited sensitivity. By further suppressing technical noise and operating at the shot-noise limit, one could achieve a  $4 \times 10^{-9}$  stability just after 100 s of averaging.

#### IV. OUTLOOK

The system presented in this paper is developed for the nEDM experiment at the PSI. However, several current developments in the field of OPMs could improve the accessibility and applicability of this technology. Recent years have shown the appearance of startup companies that specialize in the commercialization of OPMs. The focus of these companies is to make use of microfabricated vapor cells, which can be used to make chip-scale OPMs [40]. Three companies are currently developing such sensors: QuSpin, Twinleaf, and FieldLine. Of particular interest to the system presented in this paper is the gradiometer developed by Twinleaf [41]. This sensor could be used in an array similar to the one presented here. This would simplify the access to this technology. Furthermore, the research in the field of OPMs is seeing a clear shift toward more robust sensors, which can be used in a variety of environments [42]. The bandwidth of OPMs can also be improved significantly, which would allow the system to be used with ac currents of a wide frequency range [43].

The practical benefits of this system may seem limited due to the dependence on the relative sensitivity. However, many of disadvantages can be mitigated or significantly suppressed. The current at which this system operates can be changed simply by changing the coil constant. Thus, the optimal operating field for the sensors can be chosen for the current that one wants to stabilize. Compared to a DMM, the range of operation is limited, since the relative performance degrades due to gradients and nonlinearities. However, the continued progress and miniaturization of OPMs should significantly mitigate this problem [40,42].

Figure 16 shows several variations of the cubic coil geometry used in this work. The design method for this type of coil is based on the magnetic scalar potential  $\Phi_M$ . It allows us to define the desired magnetic field and compute the location of the wires required to generate this magnetic

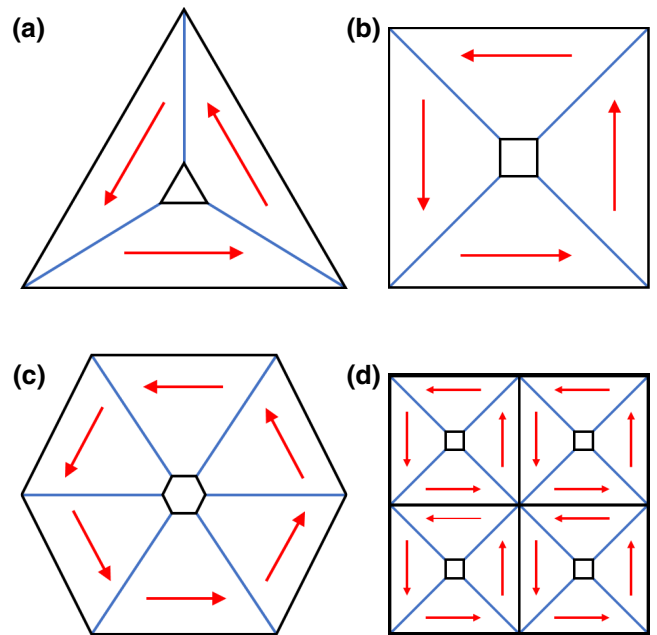


FIG. 16. A schematic representation of (a) a triangular, (b) a square, and (c) a hexagonal coil. The black boundaries represent a zero flux condition, i.e., no field can pass. The blue boundaries represent the flux conditions to guide the magnetic field from one section to the next. The red arrows represent the magnetic field direction in each section. The PCB design of these coils allows for more complex wire paths and more complex coil systems to be built. (d) These simple coils can be used as building blocks for more complex constructs.

field. For simple geometric shapes as shown in Fig. 16, the wires will always be equidistant and evenly spaced, as for the coil prototype of Fig. 2 [18]. Having more sensors at different locations will improve the discrimination feature of this system. In particular, a design such as the one shown in Fig. 16(d) would allow us to discriminate and even measure higher-order gradients. The PCB design of the coil would allow the use of card edge connectors, which makes the construction of such a coil feasible.

#### V. CONCLUSION

We present a current-monitoring system, the concept of which can be adapted to detect current variations of any current source. It features a field-confining coil, which contains four optically pumped magnetometers. This allows us to exploit the sensitivity of these magnetometers and convert the magnetic sensitivity into a current sensitivity. When the setup is well shielded and thermally stable, the sensitivity of this system is mainly limited by the sensitivity of the magnetometers. For Cs and K magnetometers operating in a free-spin-precession mode in a  $1 \mu\text{T}$  holding field, we measure a shot-noise-limited sensitivity of about  $200 \text{ fT}/\sqrt{\text{Hz}}$  and  $20 \text{ fT}/\sqrt{\text{Hz}}$ , respectively. This corresponds to a current sensitivity of  $400 \text{ pA}/\sqrt{\text{Hz}}$

and  $40 \text{ pA}/\sqrt{\text{Hz}}$ , respectively. The best performance is observed for magnetic fields larger than  $1 \text{ } \mu\text{T}$  and using Cs magnetometers. A relative sensitivity of better than  $5 \times 10^{-9}$  is achieved when the magnetic field of the coil is  $10 \text{ } \mu\text{T}$  in an actively controlled setup. For this setup, this corresponds to a 20-mA driving current, which has a stability on the 100-pA level. The stability of this system can still be improved, for example, by improving the sensitivity of the magnetometers or by using a coil with a higher coil constant to increase the relative sensitivity.

It is shown that this current-monitoring system is able to track changes in current. It can also discriminate external magnetic perturbations through the first-order gradiometer configuration in which the magnetometers are arranged. The performance of the gradiometer can be improved by reducing the distance between magnetometers or by adding more sensors to the system. Finally, the implementation of current feedback control stabilizes a current source and achieves a high sensitivity in magnetic field and current sensing over long integration times.

### ACKNOWLEDGMENTS

This work was partly supported by the Fund for Scientific Research Flanders (FWO) and Project No. GOA/2010/10 of the KU Leuven. We would like to thank the electronics workshop of the KU Leuven physics department for designing the PCB and for constructive feedback on the design of the coil used in this work.

- 
- [1] C. Abel, N. Ayres, G. Ban, G. Bison, K. Bodek, V. Bondar, E. Chanel, P.-J. Chiu, B. Clement, and C. Crawford *et al.*, in *EPJ Web of Conferences*, (EDP Sciences, Grenoble, 2019), Vol. 219, p. 02002.
- [2] C. Abel, S. Afach, N. J. Ayres, C. A. Baker, G. Ban, G. Bison, K. Bodek, V. Bondar, M. Burghoff, and E. Chanel *et al.*, Measurement of the Permanent Electric Dipole Moment of the Neutron, *Phys. Rev. Lett.* **124**, 081803 (2020).
- [3] N. F. Ramsey, A molecular beam resonance method with separated oscillating fields, *Phys. Rev.* **78**, 695 (1950).
- [4] J. Pendlebury, S. Afach, N. Ayres, C. Baker, G. Ban, G. Bison, K. Bodek, M. Burghoff, P. Geltenbort, and K. Green *et al.*, Revised experimental upper limit on the electric dipole moment of the neutron, *Phys. Rev. D* **92**, 092003 (2015).
- [5] C. Abel, S. Afach, N. Ayres, G. Ban, G. Bison, K. Bodek, V. Bondar, E. Chanel, P.-J. Chiu, and C. Crawford *et al.*, Optically pumped Cs magnetometers enabling a high-sensitivity search for the neutron electric dipole moment, *Phys. Rev. A* **101**, 053419 (2020).
- [6] G. Ban, G. Bison, K. Bodek, M. Daum, M. Fertl, B. Franke, Z. D. Grujić, W. Heil, M. Horras, and M. Kasprzak *et al.*, Demonstration of sensitivity increase in mercury free-spin-precession magnetometers due to laser-based readout for neutron electric dipole moment searches, *Nucl. Instrum. Methods Phys. Res. Sec. A: Accelerators Spectrometers Detectors Associated Equipment* **896**, 129 (2018).
- [7] D. Drung, C. Krause, U. Becker, H. Scherer, and F. Ahlers, Ultrastable low-noise current amplifier: A novel device for measuring small electric currents with high accuracy, *Rev. Sci. Instrum.* **86**, 024703 (2015).
- [8] I. Fan, R. Behr, D. Drung, C. Krause, M. Götz, E. Pesel, and H. Scherer, Externally referenced current source with stability down to 1 nA/A at 50 mA, *IEEE Trans. Instrum. Meas.* **68**, 2129 (2018).
- [9] C. A. Hamilton, Josephson voltage standards, *Rev. Sci. Instrum.* **71**, 3611 (2000).
- [10] J. P. Pekola, O.-P. Saira, V. F. Maisi, A. Kemppinen, M. Möttönen, Y. A. Pashkin, and D. V. Averin, Single-electron current sources: Toward a refined definition of the ampere, *Rev. Mod. Phys.* **85**, 1421 (2013).
- [11] T. Wagner, P. Strasberg, J. C. Bayer, E. P. Rugeramigabo, T. Brandes, and R. J. Haug, Strong suppression of shot noise in a feedback-controlled single-electron transistor, *Nat. Nanotechnol.* **12**, 218 (2017).
- [12] N.-H. Kaneko, S. Nakamura, and Y. Okazaki, A review of the quantum current standard, *Meas. Sci. Technol.* **27**, 032001 (2016).
- [13] H. Sasaki, A. Miyajima, N. Kasai, and H. Nakamura, High-stability dc-current source using NMR lock technique, *IEEE Trans. Instrum. Meas.* **1001**, 642 (1986).
- [14] C. G. Kim, E. R. Williams, H. Sasaki, S. Ye, P. Olsen, and W. L. Tew, Nuclear magnetic resonance-based current-voltage source, *IEEE Trans. Instrum. Meas.* **42**, 153 (1993).
- [15] E. B. Baker and L. Burd, High stability nuclear magnetic resonance spectrograph, *Rev. Sci. Instrum.* **28**, 313 (1957).
- [16] V. Y. Shifrin, C. Kim, and P. Park, Atomic magnetic resonance based current source, *Rev. Sci. Instrum.* **67**, 833 (1996).
- [17] G. Li, Q. Xin, X. Geng, Z. Liang, S. Liang, G. Huang, G. Li, and G. Yang, Current sensor based on an atomic magnetometer for dc application, *Chin. Opt. Lett.* **18**, 031202 (2020).
- [18] P. A. Koss, C. Crawford, G. Bison, E. Wursten, M. Kasprzak, and N. Severijns, PCB coil design producing a uniform confined magnetic field, *IEEE Magn. Lett.* **8**, 1 (2017).
- [19] C. Crawford, The physical meaning of the magnetic scalar potential, and how to use it to design an electromagnet, *arXiv:2012.00800* (2020).
- [20] E. Arimondo, M. Inguscio, and P. Violino, Experimental determinations of the hyperfine structure in the alkali atoms, *Rev. Mod. Phys.* **49**, 31 (1977).
- [21] S. Pustelny, D. J. Kimball, S. Rochester, V. Yashchuk, and D. Budker, Influence of magnetic-field inhomogeneity on nonlinear magneto-optical resonances, *Phys. Rev. A* **74**, 063406 (2006).
- [22] W. E. Bell and A. L. Bloom, Optical detection of magnetic resonance in alkali metal vapor, *Phys. Rev.* **107**, 1559 (1957).
- [23] E. B. Alexandrov and V. A. Bonch-Bruевич, Optically pumped atomic magnetometers after three decades, *Opt. Eng.* **31**, 711 (1992).
- [24] D. Budker and M. Romalis, Optical magnetometry, *Nat. Phys.* **3**, 227 (2007).

- [25] H. Robinson, E. Ensberg, and H. Dehmelt, Preservation of spin state in free atom-inert surface collisions, *Bull. Am. Phys. Soc* **3**, 9 (1958).
- [26] N. Castagna, G. Bison, G. Di Domenico, A. Hofer, P. Knowles, C. Macchione, H. Saudan, and A. Weis, A large sample study of spin relaxation and magnetometric sensitivity of paraffin-coated Cs vapor cells, *Appl. Phys. B* **96**, 763 (2009).
- [27] Z. D. Grujić, P. A. Koss, G. Bison, and A. Weis, A sensitive and accurate atomic magnetometer based on free spin precession, *Eur. Phys. J. D* **69**, 135 (2015).
- [28] E. Aleksandrov, M. Balabas, A. Vershovskii, A. Ivanov, N. Yakobson, V. Velichanskii, and N. Senkov, Laser pumping in the scheme of an  $M_x$ -magnetometer, *Opt. Spectrosc.* **78**, 292 (1995).
- [29] W. F. Avrin and R. E. Sager, An optically pumped magnetic sensor with submilligamma resolution, *IEEE Trans. Magn.* **25**, 3408 (1989).
- [30] S. Afach, G. Ban, G. Bison, K. Bodek, Z. Chowdhuri, Z. Grujić, L. Hayen, V. Hélaine, M. Kasprzak, and K. Kirch *et al.*, Highly stable atomic vector magnetometer based on free spin precession, *Opt. Express* **23**, 22108 (2015).
- [31] C. R. Rao, in *Breakthroughs in statistics* (Springer, New York, 1992), p. 235.
- [32] C. Gemmel, W. Heil, S. Karpuk, K. Lenz, C. Ludwig, Y. Sobolev, K. Tullney, M. Burghoff, W. Kilian, and S. Knappe-Grüneberg *et al.*, Ultra-sensitive magnetometry based on free precession of nuclear spins, *Eur. Phys. J. D* **57**, 303 (2010).
- [33] S. Groeger, G. Bison, J.-L. Schenker, R. Wynands, and A. Weis, A high-sensitivity laser-pumped  $M_x$  magnetometer, *Eur. Phys. J. D—At. Mol. Opt. Plasma Phys.* **38**, 239 (2006).
- [34] G. Cates, S. Schaefer, and W. Happer, Relaxation of spins due to field inhomogeneities in gaseous samples at low magnetic fields and low pressures, *Phys. Rev. A* **37**, 2877 (1988).
- [35] G. Breit and I. Rabi, Measurement of nuclear spin, *Phys. Rev.* **38**, 2082 (1931).
- [36] <http://zedboard.org/product/zedboard>.
- [37] W. J. Riley, *Handbook of Frequency Stability Analysis* (U.S. Department of Commerce, National Institute of Standards and Technology, Gaithersburg, 2008).
- [38] G. Bison, N. Castagna, A. Hofer, P. Knowles, J.-L. Schenker, M. Kasprzak, H. Saudan, and A. Weis, A room temperature 19-channel magnetic field mapping device for cardiac signals, *Appl. Phys. Lett.* **95**, 173701 (2009).
- [39] G. Lembke, S. Erné, H. Nowak, B. Menhorn, A. Pasquarelli, and G. Bison, Optical multichannel room temperature magnetic field imaging system for clinical application, *Biomed. Opt. Express* **5**, 876 (2014).
- [40] P. D. Schwindt, S. Knappe, V. Shah, L. Hollberg, J. Kitching, L.-A. Liew, and J. Moreland, Chip-scale atomic magnetometer, *Appl. Phys. Lett.* **85**, 6409 (2004).
- [41] M. Limes, E. Foley, T. Kornack, S. Caliga, S. McBride, A. Braun, W. Lee, V. Lucivero, and M. Romalis, Portable Magnetometry for Detection of Biomagnetism in Ambient Environments, *Phys. Rev. Appl.* **14**, 011002 (2020).
- [42] K.-M. C. Fu, G. Z. Iwata, A. Wickenbrock, and D. Budker, Sensitive magnetometry in challenging environments, *AVS Quantum Sci.* **2**, 044702 (2020).
- [43] N. Wilson, C. Perrella, R. Anderson, A. Luiten, and P. Light, Wide-bandwidth atomic magnetometry via instantaneous-phase retrieval, *Phys. Rev. Res.* **2**, 013213 (2020).